ACS OMEGA

Open Access

http://pubs.acs.org/journal/acsodf

Article

Hydrothermal Synthesis of Fe-Doped Cadmium Oxide Showed Bactericidal Behavior and Highly Efficient Visible Light Photocatalysis

Iram Shahzadi, Muhammad Aqeel, Ali Haider, Sadia Naz, Muhammad Imran, Walid Nabgan,* Ali Al-Shanini,* Anum Shahzadi, Thamraa Alshahrani, and Muhammad Ikram*

Cite This: *ACS Omega* 2023, 8, 30681−30693

Read Online

ACCESS | Metrics & More | Article Recommendations | Supporting Information

ABSTRACT: Cationic dyes present in industrial effluents significantly reduce the effectiveness of remediation operations. Considering the terrible impact of these pollutants on environment and biodiversity, investigating strategies to remove potentially harmful compounds from water is becoming an increasingly intriguing issue. In this work, we employed a simple hydrothermal technique to synthesize Fe-doped CdO (2, 4, and 6 wt %) nanostructures and assessed their efficacy in degrading methylene blue (MB) dye and inhibiting the growth of *Staphylococcus aureus* and *Escherichia coli*, respectively. Structural, morphological, and optical characterization of produced nanomaterials was also performed using X-ray diffraction, TEM, and UV absorption spectra. The photocatalytic decomposition of MB was significantly enhanced (58.8%) by using Fe (6 wt %)-doped CdO catalysts for 80 min under irradiation. In addition, 2.05−5.05 mm inhibitory zones were seen against Gram-positive bacteria (*S. aureus*), whereas the range for Gram-negative bacteria (*E. coli*) was 1.65−2.75 mm. These nanostructures were shown to be very effective inhibitors of beta-lactamase, D-alanine-D-alanine ligase B, and fatty acid synthase inhibitor by in silico molecular docking investigations.

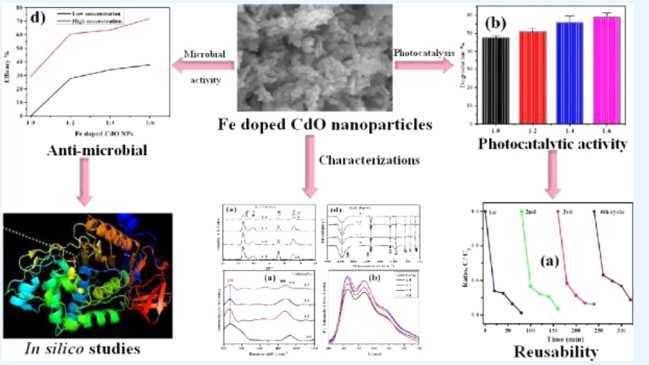

1. INTRODUCTION

Transparent conducting oxide (TCO) such as indium oxides, tin oxides, zinc oxides, and cadmium oxides exhibit considerable electrical conductivity and beneficial optical transparency, also explored as potentially useful material in optoelectronics owing to moderate impedance and significant optical reflectivity,[1−3] in addition, they are capable of producing reactive species like hydroxyl radicals that may disintegrate organic contaminants. Among the several semiconducting metal oxides available, researchers are intrigued by CdO as it is an n-type semiconductor with high binding affinity, with considerable transmission in the visible spectrum, limited resistance $\approx 10^{-2} - 10^{-4}$ Ω cm, and direct bandwidth in ∼2.2−2.7 eV region.[4,5] TCO-doped CdO offers multiple optoelectronic applications, including gas sensors, smart windows, photo-transistors, surface acoustic, photovoltaic panels, flat panel displays, translucent conductive filaments, infrared light hot mirrors, low-emissive windows, heat mirrors, narrow resistors, among others,[6,7] depending on suitable electrical conductivity and optical properties.[8] Doping CdO with metal elements such as manganese (Mn), fluorine (F), tin (Sn), dysprosium (Dy), aluminum (Al), cobalt (Co), nickel (Ni), copper (Cu), and iron (Fe) can modify its physical attributes; these dopants improve n-type conductivity and increase electrical conductivity and optical band gap.[9−13]

Doped and undoped CdO have been prepared by various processes, notably reactive sputtering,[3] chemical bath deposition, microwave irradiation,[14,15] activated reactive evaporation,[16] hydrothermal,[17] spray pyrolysis,[18] sonochemical methods,[19] chemical vapor deposition, combustion,[20] conventional precipitation,[21] and sol−gel.[22] Among these, the sol−gel method is an attractive approach for preparing metal oxide materials widely used in ceramics, catalysts, electronics, sensors, optics, and thin films. Owing to its distinctive features, this approach is intended to produce homogeneous composites with extremely high purity (99.99% purity) on an industrial scale. The lower temperature required during synthesis provides another potential benefit of this technology over conventional methods, allowing metal and ceramic nanoma-

Received: June 26, 2023
Accepted: July 28, 2023
Published: August 8, 2023

terials to be formed at temperatures between 70 and 320 °C. In contrast, the processes mentioned above generate nanomaterials at temperatures between 1400 and 3600 °C.[23−25]

The pollution of freshwater supplies and aquatic ecosystems is a pressing problem threatening human development and prosperity across globe. In recent years, semiconductor nanocomposite materials have been acknowledged as viable replacements for traditional materials for their high stability, unique physical properties, high aspect ratio, and large-surface area, all of which contribute to their superior photocatalytic performance, photovoltaic responsiveness, and potent microbicidal potential against microbes.[26] In some investigations, iron oxide nanoparticles were shown to inhibit bacterial growth by inducing reactive oxygen species (ROS), oxidative stress, and cell membrane rupture. Fe_3O_4 nanoparticle robust magnetic properties, extended endurance, high biocompatibility, low toxicity, etc., make them useful in a variety of magnetic biomedical applications, removal of heavy metal ions, and absorption of electromagnetic waves.[27] CdO nanoparticles are a photocatalyst for dye degradation[28] because of their high charge carrier mobility and excellent visible light absorption. It was recently discovered that CdO nanopowder has potent antibacterial properties. Because CdO is paramagnetic at ambient temperature, it is rarely researched as a metal oxide semiconductor.[29] Its doping with magnetic metal ions or combining it with ferromagnetic semiconductors [iron (Fe)] might boost its magnetic characteristics because Fe^{2+} ion is a somewhat smaller size than Cd^{2+} (ionic radii of Fe^{2+} and Cd^{2+} are 0.78 and 0.95 Å, respectively).[30]

According to our knowledge, there are few reports on the fabrication and evaluation of undoped and doped CdO nanopowders. This work demonstrates the hydrothermal synthesis of Fe-doped CdO nanostructures as a novel and effective antibacterial agent against *Staphylococcus aureus* bacteria. Iron (Fe) was used as a doping agent to reduce the crystallite size of prepared nanostructures, providing the large-surface area that caused to increase the antibacterial potency of CdO. Various techniques, including X-ray diffraction (XRD) patterns and FESEM, were employed for structural characteristics, while Raman and UV−vis. spectroscopies for investigating the optical properties of nanopowder samples. Furthermore, to acquire insights into a putative mechanism determining the bactericidal potential of Fe-doped CdO NPs, molecular docking investigations were conducted toward specified enzymatic targets of cell wall formation and fatty acid biosynthesis processes.

2. EXPERIMENTAL DETAILS

2.1. Materials. Cadmium acetate [$Cd(CH_3CO_2)_2{\cdot}2H_2O$, 99.0%] was acquired from Sigma-Aldrich (Germany). Iron sulfate [$FeSO_4.7H_2O$, [99.0%] and NaOH, 99.99% were obtained from Uni-Chem (India) and PenReac (Germany), respectively. Methylene blue (MB) was utilized as supplied by BDH laboratories (United Kingdom), and the chemical structure is presented in Figure 1. In present work, all chemical products obtained were in pure form and used without further purifying process.

2.2. Preparation of Fe−CdO Composites. To analyze the behavior of Fe at low concentrations, CdO/Fe (1:0, 1:2, 1:4, and 1:6) nanoparticles were synthesized via the hydrothermal method. Cadmium acetate and iron sulfate (0.5 mol L^{-1}) solutions were prepared separately in double-distilled water. Then, solutions were mixed to the prescribed quantity

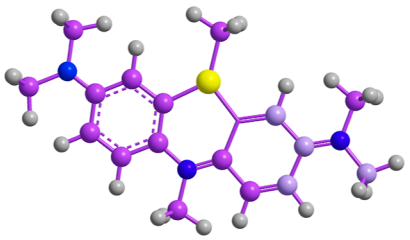

Figure 1. Chemical structure of methylene blue.

and agitated continuously at ambient temperatures (25−28 °C), along with adding 2 $molL^{-1}$ sodium hydroxide dropwise. The preceding solution was poured into a 100 mL autoclave coated with Teflon for 10 h at 160 °C in the oven and cooled at room temperature. White precipitates yielded were extensively rinsed with double-distilled water and ethanol to alleviate contaminants. The resultant was dried at 80 °C, pulverized to a powder and annealed at 500 °C for 3 h, as illustrated in Figure 2.[31]

2.3. Photocatalytic Activity. In photocatalysis,[32] produced materials were monitored by evaluating MB aqueous-solution photodegradation trend (10 mg L^{-1}). A visible radiant source of 400 W mercury lamp with wavelength 400−700 nm with lamp solution distance of about 20 cm was used. Under vigorous stirring, 50 mL of MB solution was added to 10 mg of sample powder in a beaker of equal volume (200 mL). Before the irradiation operation, the solution was agitated in the dark for 15 min to establish an adsorption−desorption equilibrium between strain and sample. The dye degradation reaction was monitored at intervals of 20 min, whereas all solutions were exposed to radiation for 80 min. UV−vis absorbance was measured using a 5 mL sample of each solution. The final degradation was evaluated by varying the maximum absorption spectrum (λ_{max} ∼ 665 nm) using an UV−vis spectrophotometer, and the mechanism is illustrated in Figure 3.

2.4. Antibacterial Activity. Pure and doped CdO nanomaterial's in vitro antibacterial performance was tested at *Escherichia coli* and *S. aureus* collected through mastitis fluid specimens. A well-diffusing test for *E. coli* and *S. aureus* in mannitol salt and MacConkey agar was conducted for in vitro microbicidal evaluation. Media plates were wiped with typical 0.5 Mc-Farland microbial cultures, and 6 mm diameter wells were formed with a sanitized borer. Each well occupied varying concentrations of pure and Fe-doped CdO (500 and 1000 μg/0.05 mL), equated with enrofloxacin as positive (5 μg/0.05 mL) and deionized water (DIW) (50 μL) as the negative control in a sterile atmosphere.

2.5. Molecular Docking Studies. The core enzymes for cell wall assembly and fatty acid biosynthesis systems have been revealed as prospective targets for the development of antibiotics. β-Lactamase, for instance, is a prominent objective of β-lactam antibiotics because its inhibition disrupts cell wall synthesis.[33,34] In this, β-lactamase and D-alanine-D-alanine ligase B (ddlB) from cell wall formation[35] along with fatty acid synthase inhibitor (FabI) of fatty acid synthesis pathway[36] were specified as promising targets for in silico docking analyses to ascertain the potential mechanism of Fe-doped CdO NPs for *S. aureus*.

The 3D structure of chosen enzyme targets was retrieved from the protein data bank using PDB IDs: 1MWU for β-lactamase*S. aureus* (resolution: 2.6 Å),[37] 5TW8 for ddlB*S. aureus* (resolution: 1.7 Å)[38] and 4CV1 for FabI*S. aureus*

https://doi.org/10.1021/acsomega.3c04543
ACS Omega 2023, 8, 30681−30693

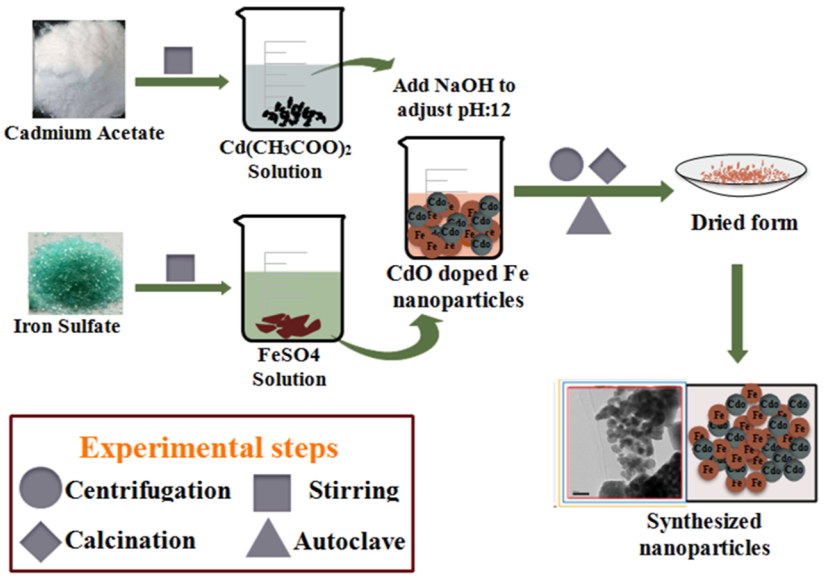

Figure 2. Schematic representation of the preparation of Fe−CdO samples.

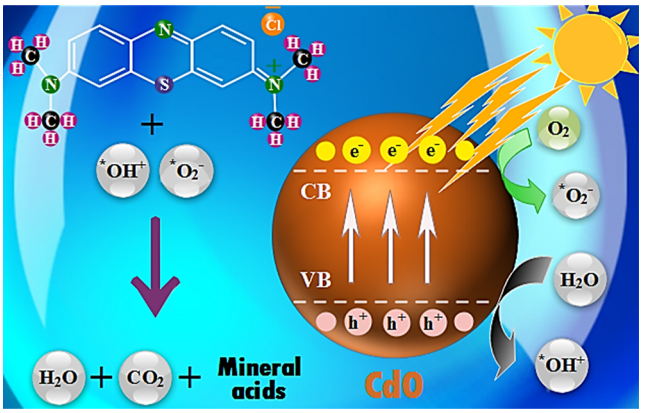

Figure 3. Photocatalysis by harvesting mechanism visible light.

(resolution: 1.9 Å).[39] The programme ICM Molsoft was employed in docking investigations.[40] Using ICM receptor preparation tool and energy minimization tool, crystal structures for docking investigations were generated and optimized separately. Water molecules in crystal structures and native ligands [i.e., (2*R*,4*S*)-2-[(1*R*)-1-{[(2,6-dimethoxyphenyl)carbonyl]amino}-2-oxoethyl]-5,5-dimethyl-1,3-thiazolidine-4-carboxylic acid for β-lactamase, ceftaroline for ddlB and 1-(3-amino-2-methylbenzyl)-4-[2-(thiophen-2-yl)ethoxy]pyridin-2(1*H*)-one for FabI] were eliminated. The active site was designated via a grid box encompassing the co-crystallized ligand. In each, the top 10 docked conformations were determined. Each produced conformation was evaluated with the optimal binding affinity, and the least binding score was chosen for further study. Discovery studio visualizer[41] and PyMOL were employed for docked complex 3D interaction study. The structure of Fe-doped CdO NPs was fabricated by modifying the CdO crystal structure acquired from PubChem by applying the ligEdit tool of ICM.

2.6. Statistical Analysis. The statistical study of the antimicrobial potency, measured using inhibition regions (mm), was performed through one-way variance analysis by SPSS 20. All experiments were performed in triplicate.

3. RESULTS AND DISCUSSION

The XRD spectra of pristine and doped CdO samples, as depicted in Figure 4a, were performed to examine Fe influence on structural and phase composition analysis of host lattice CdO. Peaks situated at 2θ = 33.25, 39.02, 56.17, 65.96, and 68.92 were indexed to (111), (200), (220), (311), and (222) planes consecutively and match JCPDS# 73-2245 well.[42] The XRD spectra presented cubic and polycrystalline structures of CdO and Cd^{2+}, which may be replaced by Fe^{2+} ions at octahedral coordination.[15] The addition of Fe into CdO caused peaks to move slightly toward lower θ values, which may be attributed to a slight change in the cadmium crystal lattice constant that could be owing to the difference in atomic radii or some intrinsic crystal defects. So, this confirms the successful incorporation of Fe into the crystal lattice.[43] The Debye Scherrer formula computed the crystallite diameter: $D = k\lambda/\beta\text{Cos}\theta$, where k is the shape factor (0.9), θ is the peak Bragg's angle, λ is the X-ray radiation wavelength (1.54 Å), and β is the broadening of diffraction line measured at peak full width of half maximum (fwhm). Calculated crystallite size decreased (45−31 nm), and the broadness of peaks enhanced with an increasing amount of dopant material attributed to lower radii of Fe^{2+} ions than Cd^{2+}, leading to a decline in the lattice gap. It can cause modification in crystallite behavior.[44] Figure 4b,c represents selected-area electron diffraction (SAED) images for pure and 4% Fe−CdO nanomaterials with four concentric well-defined spotty rings attributed to the (*hkl*) values of (111), (200), (220), and (311) planes which define high crystalline nature and polycrystalline behavior of nanomaterials and are well consistent with XRD results.

To analyze the chemical bond structure, the FTIR technique is the most common, which recorded spectra of pristine and doped samples in the 4000 to 500 cm^{-1} range, as shown in Figure 4d. The band nearby 680 cm^{-1} is ascribed to the Cd−O stretching vibration.[42] The signal at 3420 cm^{-1} is related to the OH stretching vibration of atmospherically absorbed water molecules, while at 2355 and 1626 cm^{-1}, it attributes to the adsorbed CO_2 and C−O vibrations, respectively.[45] A modest band around 1419 cm^{-1} corresponds to the bending mode of $-CH_3$, in which CO_2 and water molecules may have been

https://doi.org/10.1021/acsomega.3c04543
ACS Omega 2023, 8, 30681−30693

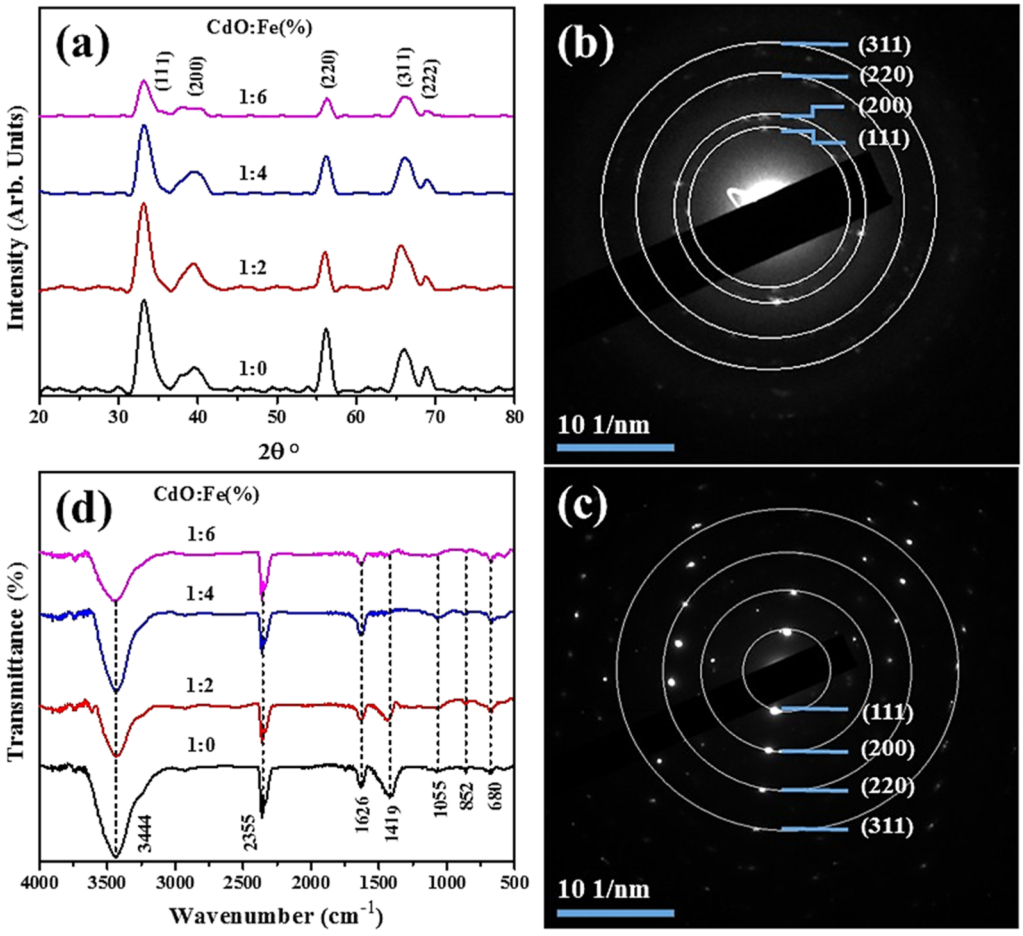

Figure 4. (a) XRD of synthesized pure and Fe-doped CdO (2, 4, and 6 wt %) products, (b,c) SAED images of undoped and 4% Fe−CdO samples and (d) FT-IR observed graphs.

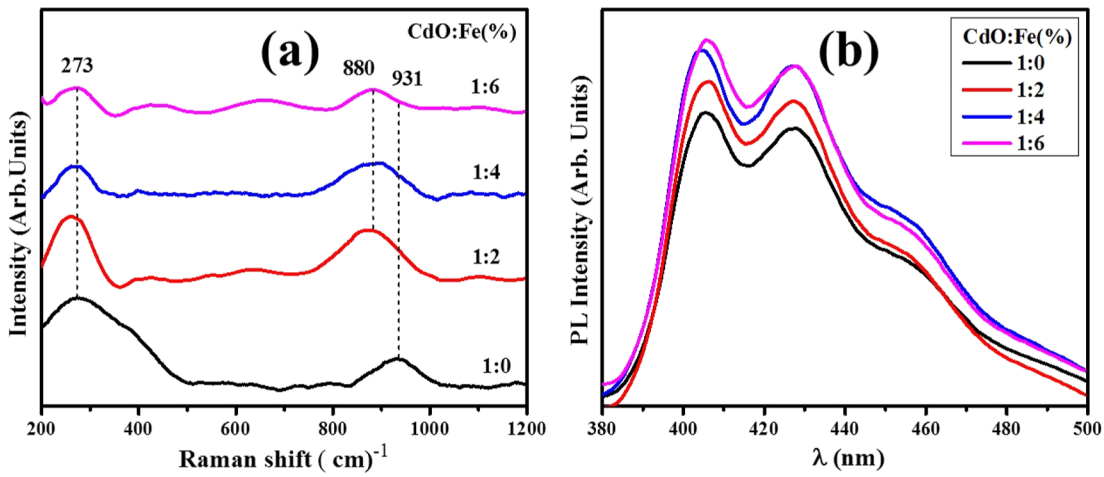

Figure 5. (a) Raman spectra of CdO and Fe-doped CdO products and (b) PL spectra.

formed in the air during its synthesis.[46] The band range from 700 to 500 cm^{-1} in pure and doped samples correspond to metal−oxygen stretching vibrations.[47]

Dynamic studies of the lattice structure provide key phonon mode information about high-quality nano-products. Raman scattering is a vital characterization technique to investigate semiconductor products and structures. Figure 5a shows Raman spectra in the 200−1200 cm-1 range of CdO and Fe−CdO nanostructures at room temperature. As reported in available articles, CdO presents Raman modes at 273, 880, and 933 cm^{-1}.[49] In principle, according to structural rocksalt selection principles, both longitudinal optical (LO) and transverse optical (TO) modes are dipoles forbidden. In the CdO spectrum, all features could be assigned to second-order Raman scattering.[48] Recently, the calculated two-phonon density of states has a discrete band of 273 cm^{-1} and 2 TA mode at the *L* point of Brillouin zone (BZ) of CdO. A large curve at 931 cm $^{-1}$ is observed as a 2LO mode overtone at

https://doi.org/10.1021/acsomega.3c04543
ACS Omega 2023, 8, 30681−30693

BZ's C- or *L*-point. The 2LO (L)-band changes to a reduced energy level and becomes broad. The possible reason for this shift may be a decrease in nanostructure size upon doping.[50] According to Thema et al., the above transverse and longitudinal modes of CdO with internal compressive stress may be manifested in the induced surface effect.[51]

Figure 5b represents the PL spectra of CdO and Fe-doped CdO nanomaterials, which depict distinct emission peaks at 411 and 428 nm and a broad band at 458 nm. The position and shape of detected bands at 411, 428, and 458 nm of pure and doped nanomaterials are almost the same. The 428 nm emission peak may be manifested in an e^- and h^+ combination.[52] The emission peak originates from electron transition from shallow donor level formed by CdO/Fe interstitials to shallow acceptor level formed by CdO/Fe vacancies. It can be attributed to the radiative recombination of a photo-generated hole with an electron occupying the oxygen vacancy on the surface of nanostructures.[53] In contrast, the 408 nm band is corresponded to near band edge or band edge emission. In contrast, depending on the particles' size the 408 nm band corresponds to near band edge or band edge emission.[54] The 458 nm shoulder peak is assigned to deep trap or surface-state emission.[55] Pure CdO possessed lower PL intensity, suggesting a low recombination rate that ascribed to phosphorescence phenomena. Upon Fe doping, PL intensity was increased, indicating the high recombination rate or low separation capacity of the electron hole pair.[56] It has been observed that doped samples' PL intensity is increased compared to pure CdO, which may be attributed to the fact that as Fe-doped CdO samples are illuminated, and more electron−hole pairs are generated. The immediate recombination of produced pairs provides more photons, resulting in high PL intensity.

Morphological analysis of CdO products was investigated via FESEM, as depicted in Figure 6a. The FESEM image of (pure)

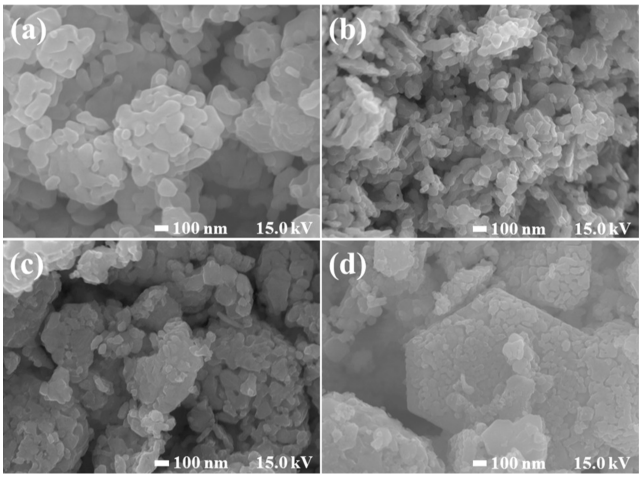

Figure 6. FESEM of (a) CdO and (b−d) Fe (2, 4, and 6) wt % induced CdO.

CdO represents nearly spherical agglomeration of particles. Figure 6b−d depicts the increase in particle agglomeration and non-uniform distribution upon doping. The van-der Waals forces produce the common agglomeration phenomenon.[56,57]

Furthermore, compositional analysis and quality of synthesized nanoparticles were determined using the EDS spectrum. As shown in Figure 7, CdO and Fe (2, 4, and 6 wt %) embedded CdO nanoparticles composed of Cd, O, and dopant element Fe along with the small content of Cu. Zn and Na were owing to contaminants. The Fe peaks in EDS images of samples endorse Fe doping into the CdO lattice structure. For FESEM analysis, Cu coating of fabricated products was found responsible for the impurity peak of Cu in the present study.[32]

The HR-TEM micrographs reveal nanomaterial size, morphology, and effect of Fe on CdO nanoparticles. Figure 8a,b and insets depict nanosized grains and tiny pores in CdO samples. In pure CdO HR-TEM image, particles are agglomerated and mixed; upon doping of Fe to CdO image (Figure 8b) showed nanosized nearly spherical agglomerated grains can be observed manifested to magneto−static interactions among nanoparticles by Fe^{2+} content incorporation, which is in agreement with SEM results. In Figure 8c,d, nanoparticle lattice fringes represent interplanar distances 0.231 and 0.267 nm, which correspond to (111) and (200) crystal planes of CdO nanoparticles, respectively,[58,59] indicating that Fe content is well mixed into CdO host lattice and agrees with XRD analysis.

UV−vis spectra of CdO and doped CdO samples are presented in Figure 9a. To observe absorbance analysis for the spectral range 250−900 nm at room temperature, an aqueous solution of nanoparticles was obtained under ultrasonication. The absorption spectrum of CdO depicts a sharp peak at ∼297 nm attributable to excitonic absorption behavior for the host lattice (CdO).[60] The absorption spectra of doped nanomaterials revealed a slight increase in light absorbance compared to pure CdO. Study samples' nature and band gap energy values were calculated using correlation among absorption-coefficient (denoted by α). Incident photon energy (presented by $h\nu$): $(\alpha h\nu)1/n = A(h\nu - E_g)$, where E_g represents the material optical band gap energy and α represents the absorption coefficient. It stands for constant, and n contains a 1/2 (direct band gap) or 2 (indirect optical-band gap) value.[61] Direct band-energy of undoped and doped-CdO nanomaterials was observed from energy graph $((\alpha h\nu)^2$ vs E) by extrapolation on the *x*-axis. CdO band gap value is 3.28 ± 0.02 eV;[62,63] the increase in the band gap value for CdO samples indicates that the interfaces of Cd and O are effectively incorporated, along with particle size and lattice or surface defects. CdO exhibits lattice defects such as oxygen vacancies and quantum confinement effect. In contrast, doped products range from 3.14 to 2.96 eV with 0.04 to 0.76% error (Figure 9b). Thus, the doping process improves the optical transparency of host material CdO and decreases the band gap of doped samples, and further Fe content in CdO may decrease in the band gap value [45,55]. The decrease in optical band gap may be related to the Burstein-Moss effect, which states that the CdO absorption edge is shifted toward lower band gap values. This effect arises when carrier content exceeds the conduction band edge density of states via Fe doping in host material.[44] The other reason for the band gap energy decrease was the semiconductor nature of CdO samples, and oxygen deficiency in CdO structure may be fulfilled by Fe ions, making it more conducting. This phenomenon is common in nanoscale materials such as pure and doped CdO.[64]

In dye degradation, photocatalyst quantity, morphology, surface zone, and irradiation time are key elements that might impact specific dye degradation efficacy.[65] Photoactivity for purified CdO and Fe (2, 4, and 6 wt %)-doped CdO were investigated through MB decomposition under a specific light source upon adsorption/desorption achieved in darkness for

https://doi.org/10.1021/acsomega.3c04543
ACS Omega 2023, 8, 30681−30693

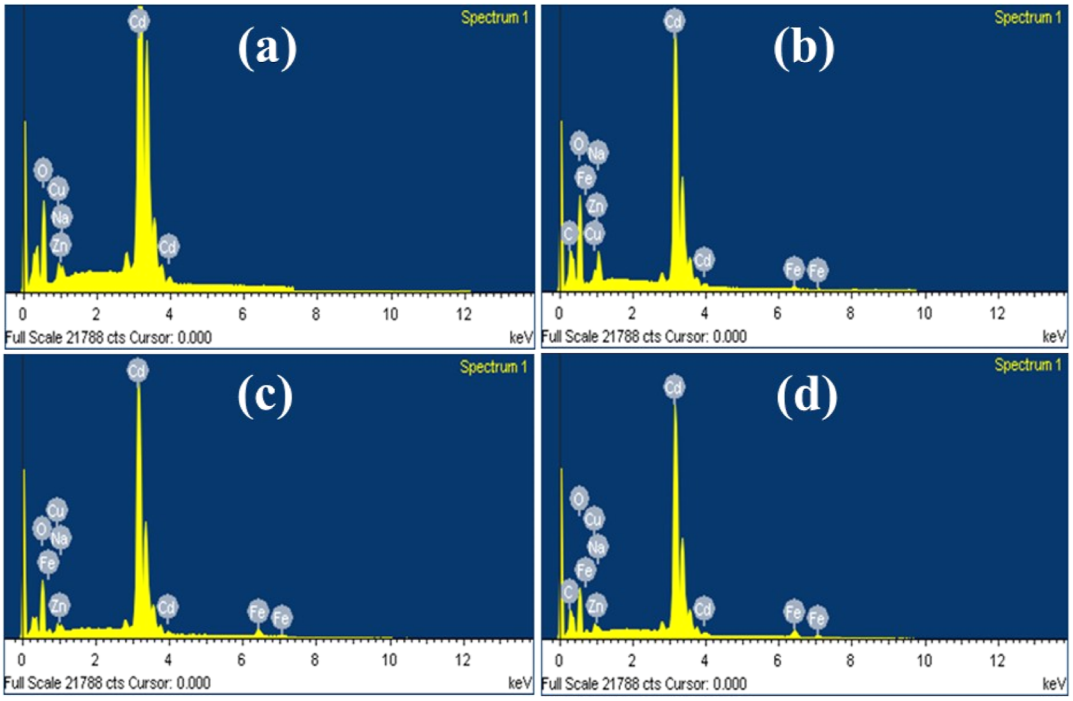

Figure 7. EDX spectra of (a) CdO and (b–d) Fe (2, 4, and 6) wt %-induced CdO.

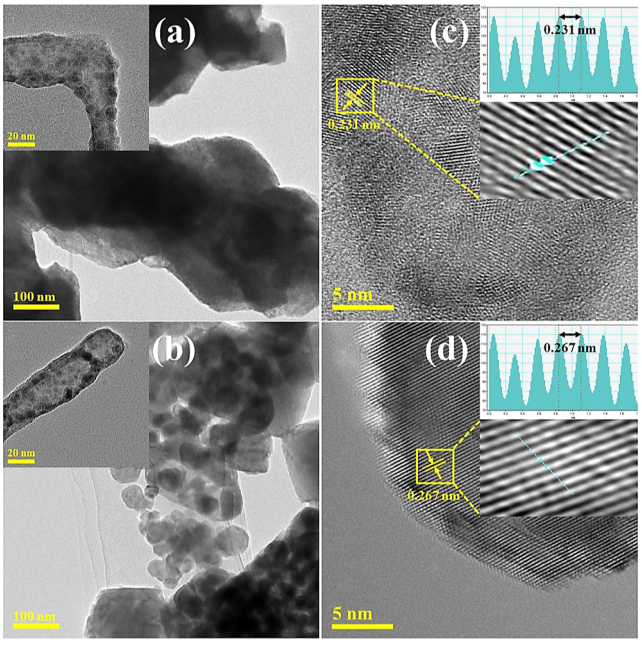

Figure 8. (a,b) HR-TEM images and (c,d) lattice fringes of pure and (4%) Fe-incorporated CdO nanomaterials, respectively.

15 min. Removal of dye was examined by the graph among illumination time vs MB concentration (C/C_0), as depicted by Figure 10a. Following irradiation, both CdO (pure and doped) decomposed MB within 80 min. At the same time, undoped CdO had the lowest decomposition efficiency (47.5%), as indicated in Figure 10b. Intriguingly, the Fe (6 wt %)-doped CdO sample acquired the highest degradation percentage % (58.8%). Result revealed 1:6 specimens as potential luminous photocatalysts manifested by a reduced bandwidth and charge-carrier recombination. The other reason for high degradation of doped CdO may be the transition metal Fe, which provides better confinement of electrons upon irradiation that slow down the recombination of excitons.[64] In Fe-doped CdO samples, Fe exists in the Fe^{3+} or Fe^{2+} form, and these ions further increase the probability of capturing electrons. At the beginning of the process, rapid desorption was observed owing to an abundance of binding sites on a large surface of products and slowed down when MB dye residual degradation took place.[66,67] Furthermore, the linearity of Ln (C_0/C) and irradiation time (Figure 10c) was employed to improve a first-order kinetic model for degrading kinetics, as detailed below

$$\ln(C_0/C) = kt \quad (1)$$

where k is the apparent rate constant and C_0 and C are concentrations for pollutant (mg L^{-1}) in DIW at t_0 and t times, respectively. The calculated values of k of pure and doped CdO during irradiation source are 0.1414, 0.1492, 0.1776, and 0.1923 $(min)^{-1}$. Rate constants and MB photodegradation values of Fe-doped CdO obtained considerable improvements. The improvement in the value of k is due to a decrease in the band gap of nanomaterials, and lower band gap materials can harvest more light for photocatalysis. As depicted in Figure 10a, CdO nanoparticles degraded a large amount of pollutant during the first 20 min, and then, the degradation process occurred slowly. Due to the (nonlinear degradation behavior of CdO with respect to the time) dependence of degrading kinetics on Figure 10a data, the linear fit line graph deviated from the initial points.

To verify durability and recyclability, the 1:6 nanomaterial was subjected to light source exposure for up to four cycles for photo-decomposition of MB from contaminated water. After four sequential cycling photo activities (Figure 11a), nanoparticles turn off contaminant colorant removal under identical conditions. Figure 11b illustrates that the degradation % of the product decreased from 58.8 to 51.3% after four cycles prescribed for photocatalyst loss via rinsing/centrifugation in

https://doi.org/10.1021/acsomega.3c04543
ACS Omega 2023, 8, 30681−30693

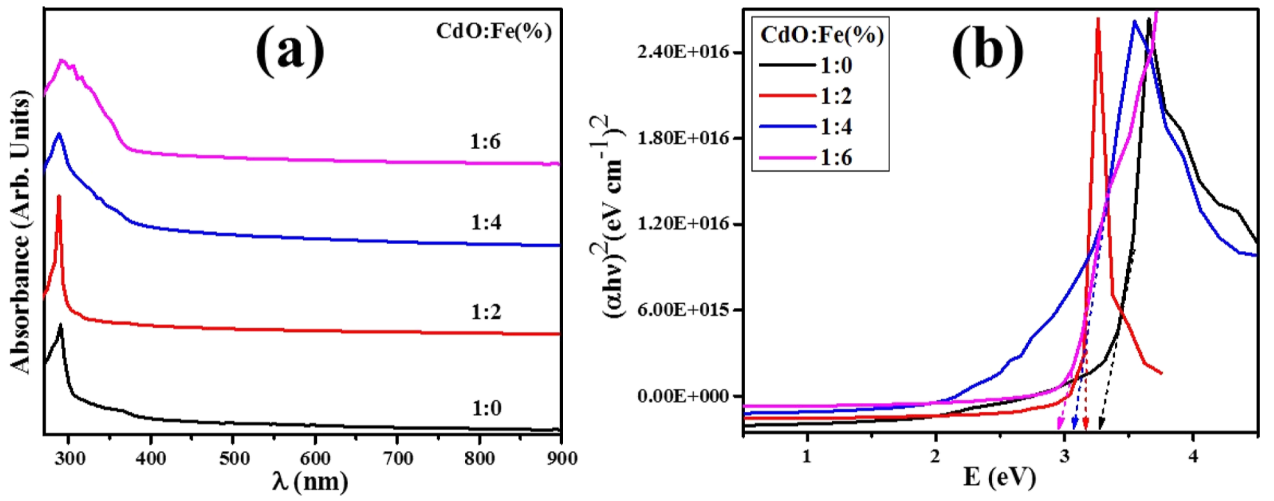

Figure 9. (a) UV−vis spectra and (b) direct band gap of pristine and Fe-doped CdO products.

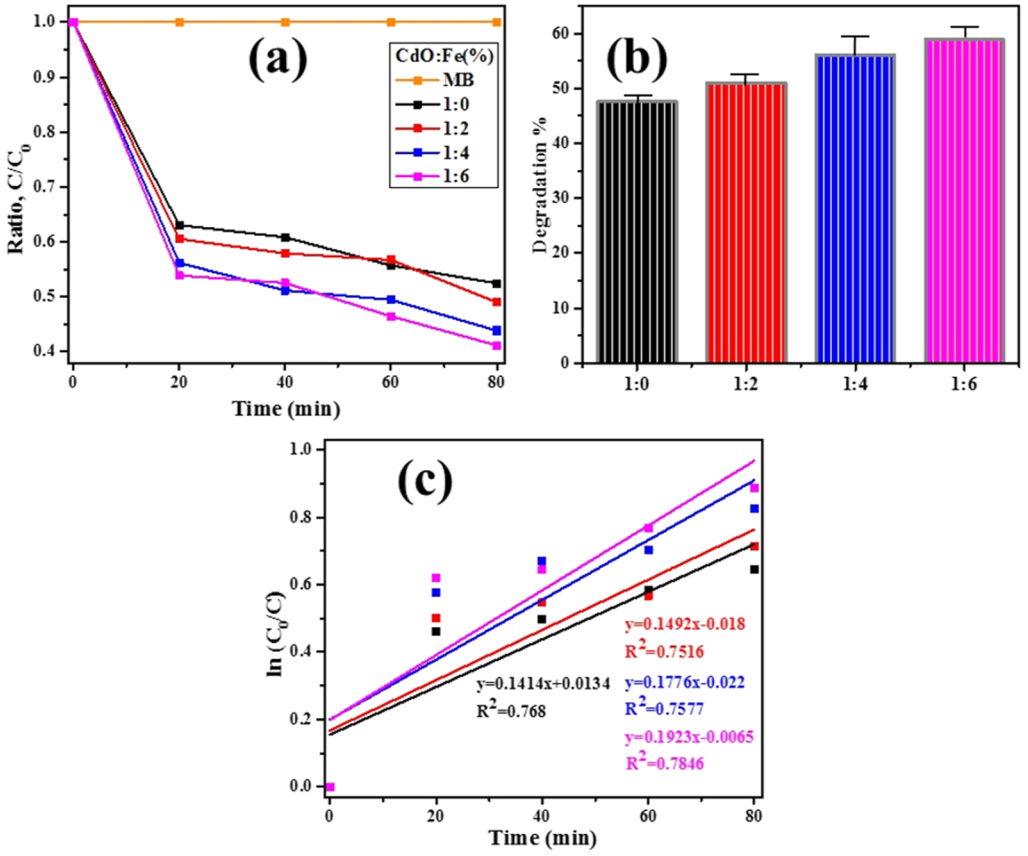

Figure 10. (a) Plot between C/C_0 versus irradiation time, (b) degradation % graph, and (c) $\ln(C_0/C)$ versus illumination time.

recycling trials. According to recycling test results, photocatalysts were relatively robust and exhibited substantial potential for polluted water treatment. The degree of mineralization was estimated by measuring total organic carbon (TOC) in treated water. The investigation was conducted on Fe-doped CdO nanostructures (2, 4, and 6 wt %) at various time intervals of up to 150 min. This investigation (Figure 11c) indicated that the TOC of produced compounds under visible light irradiation decreased steadily with reaction time, and a considerable quantity of mineralization of dye was noticed after 150 min in Fe (6 wt %)-doped CdO. Moreover, results suggest that the dye may undergo a series of intermediate transformations before its deterioration ultimately leads to its complete mineralization.[68,69] The comparison of the current work with the literature, in terms of photocatalytic activity and reaction time is shown in Table 1.

If photocatalytic efficacy of prepared Fe−CdO nanostructures was considered in terms of duration of the degradation rate, then Fe−CdO showed significant photocatalytic activity as compared to TiO_2, WO_3, and ZnO (Figure 12).[73−76] The degradation rate of the prepared nanostructures can be calculated by eq 2.

https://doi.org/10.1021/acsomega.3c04543
ACS Omega 2023, 8, 30681−30693

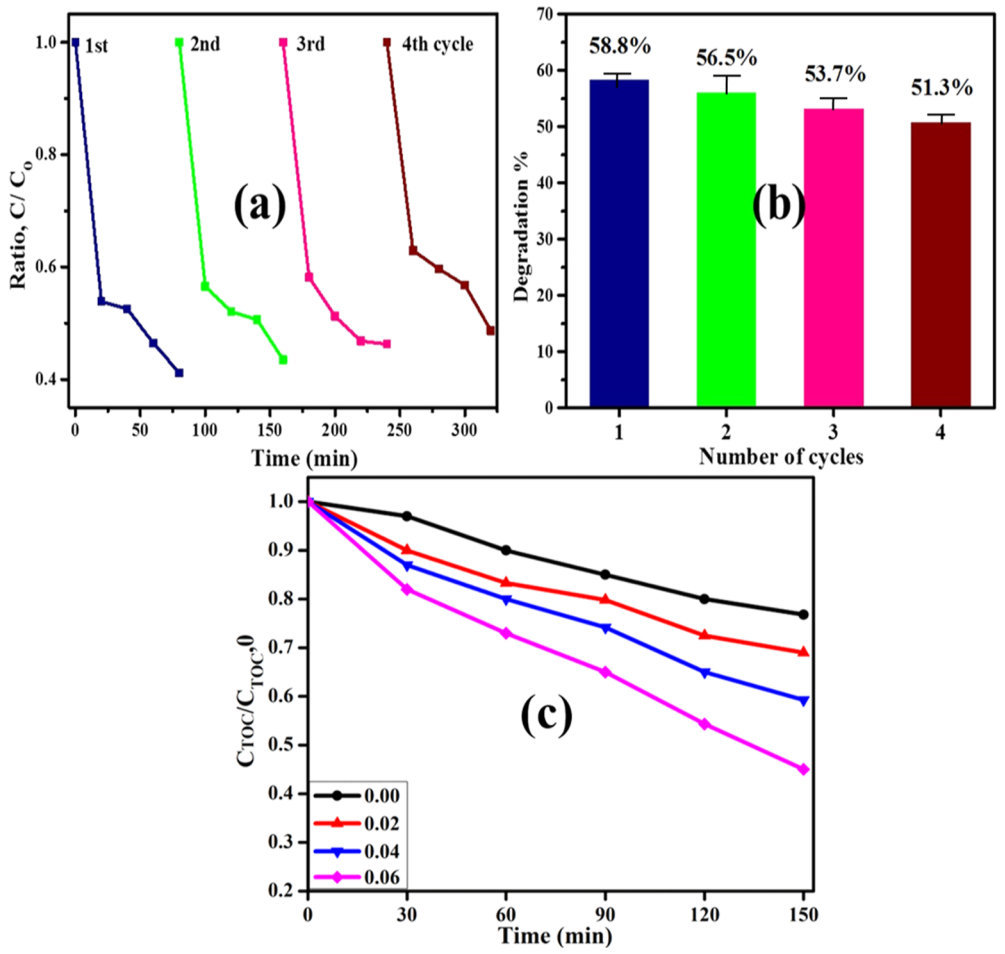

Figure 11. (a) Fe (6 wt %)-doped CdO nanostructures reusability and (b) degradation % bar graph. (c) TOC of synthesized nanostructures.

Table 1. Comparison of Synthesized Nanostructures Degradation Efficacy with the Literature

photocatalyst	degradation efficiency (%)	reaction time (min)	dyes	ref
Bi_2CrO_6	56	120	MB	70
CeO_2	34.24	120	MB	71
SnO_2	79	840	MB	72
Ag/TiO_2	51.18	180	MB	73
TiO_2	100	300	MB	74
WO_3	80	180	Methyl orange	75
ZnO	85	120	Phenol	76
$CdO-Fe_3O_4$	92.85	150	MB	42
γ-Fe3/ Fe_3O_4/SiO_2	87.5	120	MB	77
CdO−NiO	89.44	180	Methyl orange	78
Fe−CdO	58.8	80	MB	present study

$$\%\ \text{degradation rate} = \frac{(C_0 - C_t)/C_0}{t} \times 100 \quad (2)$$

The in vitro microbicidal effectiveness in pure and doped bacteria samples was examined using a well diffusion analysis for measuring inhibition areas, with respective (half minimum inhibitory concentration) IC_{50} values shown in Table 2 (Figure 13a−d) and Table 3. Data collected from both samples revealed antibacterial activity. Findings demonstrated a

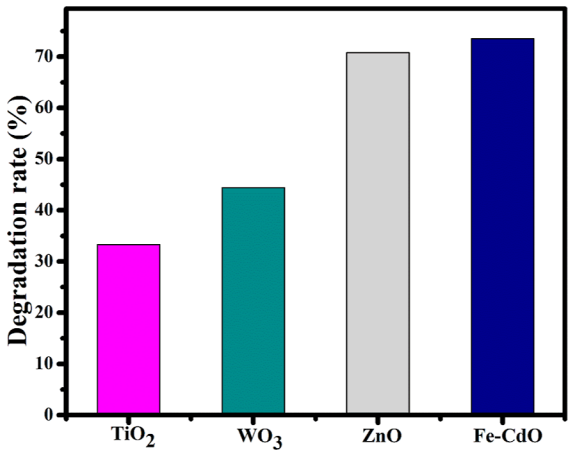

Figure 12. Photocatalytic activity of TiO_2, WO_3, ZnO, and Fe−CdO nanostructures in terms of the percentage degradation rate.

synergistic impact between specimens produced and inhibition areas. Statistically, substantial inhibition regions ($p < 0.05$) for small and large concentrations against *E. coli* ranged (0.9 ± 0.01 to 1.4 ± 0.06 mm) and (1.65 ± 0.02 to 2.75 ± 0.07 mm), whereas (0 ± 0.0 to 2.65 ± 0.05 mm) and (2.05 ± 0.02 to 4.9 ± 0.06 mm) for *S. aureus* were attained in case of doped CdO nanostructures, correspondingly (Table 2). All outcomes were equated with enrofloxacin (4.30 ± 0.03 mm) and (7.0 ± 0.04 mm) for *E. coli* and *S. aureus*, correspondingly, and with DIW

https://doi.org/10.1021/acsomega.3c04543
ACS Omega 2023, 8, 30681−30693

Table 2. Antibacterial Action of Fe−CdO

samples	inhibition zone (mm)[a]		inhibition zone (mm)[b]	
	500 μg/50 μL	1000 μg/50 μL	500 μg/50 μL	1000 μg/50 μL
1:0	0.9 ± 0.01	1.65 ± 0.02	0 ± 0.0	2.05 ± 0.02
1:2	1.1 ± 0.05	2.15 ± 0.04	1.95 ± 0.03	4.25 ± 0.03
1:4	1.25 ± 0.08	2.3 ± 0.05	2.4 ± 0.04	4.45 ± 0.05
1:6	1.4 ± 0.06	2.75 ± 0.07	2.65 ± 0.05	4.9 ± 0.06
enrofloxacin	4.30 ± 0.03	4.30 ± 0.03	7.0 ± 0.04	7.0 ± 0.04
DIW	0 ± 0.0	0 ± 0.0	0 ± 0.0	0 ± 0.0

[a]Inhibition areas of Fe-doped CdO for Gram-negative bacteria. [b]Measurements of zones of inhibition (mm) against Gram-positive bacteria.

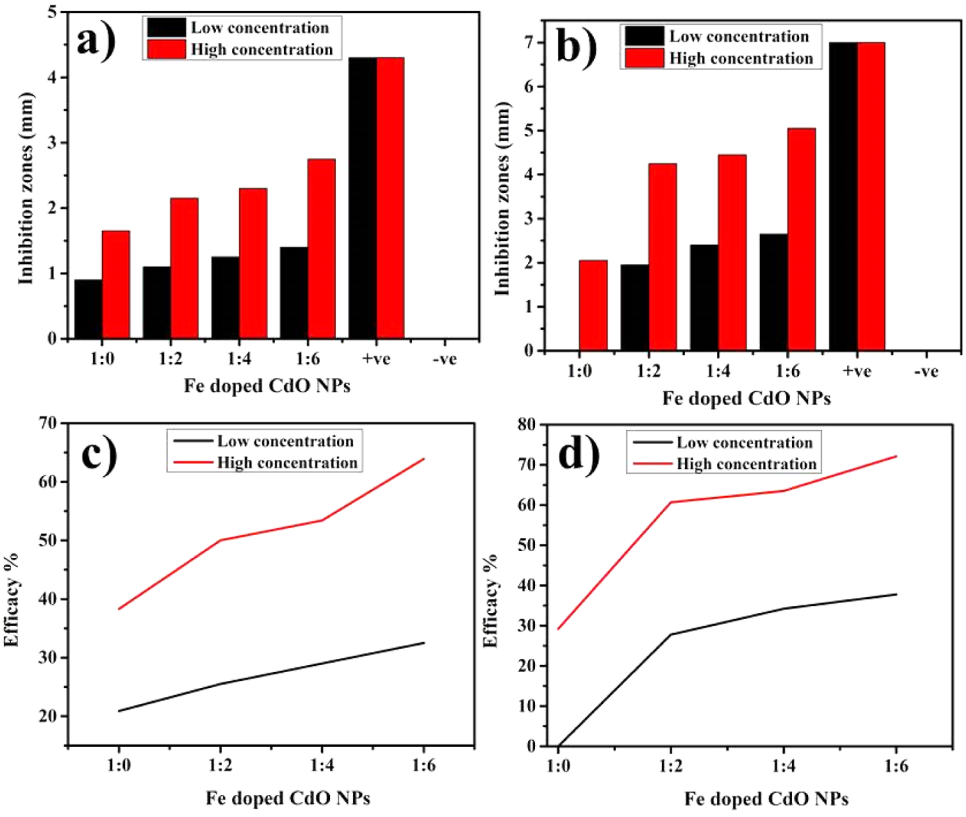

Figure 13. (a) In vitro antibacterial action of Fe−CdO for *E. coli* and (b) *S. aureus*. (c) Efficacy % age for Gram-negative (d) and Gram-positive bacteria, respectively.

Table 3. IC_{50} of Fe−CdO High Concentrations

samples	E. coli	S. aureus
	μg/mL	μg/mL
1:0	4	2
1:2	2.84	1.44
1:4	1.35	1.15
1:6	0.62	0.43
enrofloxacin	0.27	0.15

(0 ± 0.0 mm) (Figure 13a,b). Overall, the efficacy % age of doped samples increased from 25.5 to 32.5% and 50 to 63.9% for *E. coli* and 27.5−37.8% and 60.7−70% for *S. aureus* at least and maximum concentrations, correspondingly. Broadly, Fe (6 wt %)-doped CdO sample exhibited superior bactericidal efficacy against *S. aureus* in contrast with *E. coli* at both concentrations. Fe-doped CdO exhibited marvelous antibacterial efficacy for Gram-positive as compared to Gram-negative bacteria (Figure 13c,d). The antibacterial strength of nanoparticles is mediated by the scale and concentration of manufactured nanostructures.[79,80] The bacteria are enclosed externally by ROS, and bacterial death is carried out by the extrusion of cell organelles.[81,82] Micro pathogens often collapse as cations associate strongly with negative microbial cell components. Differences in bacterial cell wall architecture may account for the improved bactericidal activity. G −ve microbes have a thinner peptidoglycan coating in their cell wall and an exterior membrane made of proteins and phospholipids, whereas G +ve bacteria have a robust layer of peptidoglycan made of lipoteichoic and teichoic acids in the outer wall.[83] Micro pathogenic failure occurs when cations induce dysfunction and enzyme degradation in bacterial ribosomal activity.[84] The production of ROS and the release of Cd^{2+} ions are two variables that contribute toward the antibacterial efficacy of both pure and doped CdO samples. Since bacteria have a negatively charged cell membrane, they have a substantial electrostatic interaction with them and allowing for piercing the membrane and causing harm. When CdO nanoparticles come into touch with bacteria, Cd^{2+} ions are

https://doi.org/10.1021/acsomega.3c04543
ACS Omega 2023, 8, 30681−30693

liberated from the particle's surfaces and are taken up by the bacteria through their transport mechanisms.[85]

Metal-doped nanoparticles have been documented as good microbicidal agents. Their bactericidal potential is attributed to either cell wall disintegration or suppression of critical biochemical processes necessary for bacterial survival and development.

3.1. Molecular Docking Analysis. Enzymes have been reported as the main virulence factor, and inhibiting their activity will disrupt essential cell processes and ultimately cause bacterial death. Keeping in view the good antibacterial activity of Fe-doped CdO NPs in the current study, we performed in silico docking investigations to evaluate their inhibition tendency against enzymes (β-lactamase and ddlB) from the cell wall biosynthetic route along with FabI from the fatty acid biogenesis. Exploring the mechanism governing the bactericidal activity of NPs is essential and will open new horizons for doped nanoparticles as antibiotic agents.

First enzyme β-lactamase that is required in cell wall biosynthesis pathway showed an excellent binding score of −7.571 kcal/mol for Fe doped CdO NPs and key amino acids of binding pocket implicated in H-bonding interactions were Gln521 (3.0 Å), Tyr519 (3.2 Å), and Asn464 (2.1 Å), as shown in Figure 14 a and b. Similarly, good binding

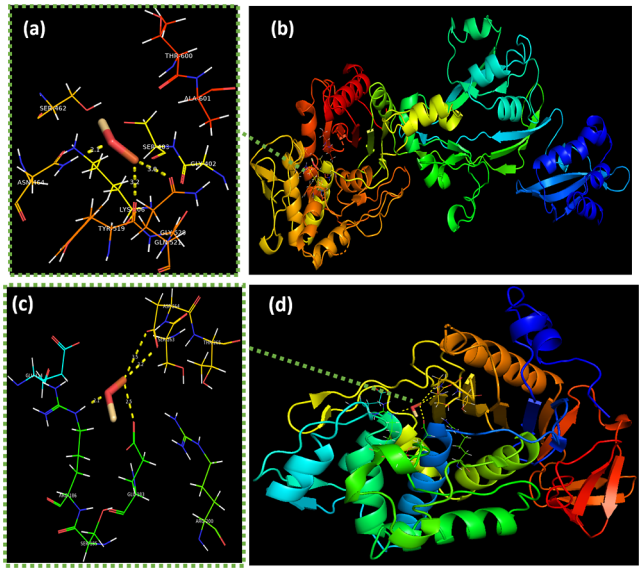

Figure 14. Binding interaction pattern of Fe-doped CdO NPs against selected cell wall synthesis enzymes (a,b). β-Lactamase and (c,d). ddlB from *S. aureus*.

interactions, i.e., H-bonding with Asp264 (3.2 Å and 3.5 Å), Glu183 (2.5 Å), and Arg186 (2.1 Å), were observed inside the active pocket of ddlB enzyme (binding score −5.881 kcal/mol), as depicted in Figure 14c and d.

The optimally docked complex of Fe-doped CdO NPs against FabI exhibited H-bonding interactions with Gly104 (2.2 Å), Arg103 (3.1 Å), and Asn158 (2.0 Å) and a binding score of −5.981 kcal/mol (Figure 15a,b). Fe-doped CdO interactions inside specified enzymes of cell wall biosynthesis and fatty acid biogenesis are predicted as potential inhibitors that are further suggested to be confirmed through enzyme inhibition studies.

Using computational tools to explore new drug candidates and novel antibiotics has replaced the traditional method of

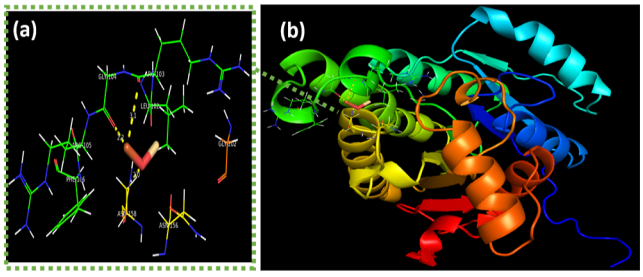

Figure 15. Binding interaction pattern of Fe-doped CdO NPs against Enoyl-[acyl-carrier-protein] reductase (FabI) from *S. aureus*.

drug discovery. As molecular docking studies enabled the in-depth analysis of inhibitor−enzyme complexes here, we identified these synthesized NPs as potential inhibitors for beta-lactamase and ddlB enzyme, as evidenced by their tendency to bind inside active pockets.

4. CONCLUSIONS

A cost-effective and environmentally favorable hydrothermal method was adopted to effectively prepare Fe-doped CdO nanomaterials with varying Fe concentrations (2, 4, and 6 wt %) to evaluate their microbicidal and dye degradation potential. XRD analysis revealed the cubic structure of CdO and iron (Fe) used as a doping agent reduces the crystallite size of the prepared nanostructures from 45 to 31 nm. The FTIR spectra exhibited metal−oxygen stretching vibrations between 700 and 500 cm^{-1}, while elemental composition confirmed the presence of Fe, Cd, and O. However, doped nanomaterials displayed a significant decrease in band gap from 3.28 eV (CdO) to 2.82 eV (0.06), evidenced by the UV spectra. The formation of electron−hole pairs by Fe-doped CdO nanoparticles allowed them to play a crucial role in removing MB dye, with maximum photodegradation efficiency attained 58.8% after 80 min in MB aqueous solution when subjected to a specific irradiation source. The degradation % of 0.06 sample reduced from 58.8 to 51.3% after four cycles, demonstrating these nanostructures a stable photocatalyst. In addition, Fe-doped CdO exhibited efficient antibacterial efficacy for Gram-positive bacteria, and in silico molecular docking studies predicted inhibition of β-lactamase, D-alanine-D-alanine ligase B (ddlB), and FabI enzymes as a possible mechanism behind the antibacterial activity of Fe-doped CdO NPs.

■ ASSOCIATED CONTENT

Supporting Information

The Supporting Information is available free of charge at https://pubs.acs.org/doi/10.1021/acsomega.3c04543.

BET analysis (PDF)

■ AUTHOR INFORMATION

Corresponding Authors

Walid Nabgan − *Departament d'Enginyeria Química, Universitat Rovira I Virgili, Tarragona 43007, Spain;* orcid.org/0000-0001-9901-862X; Email: wnabgan@gmail.com

Ali Al-Shanini − *College of Petroleum and Engineering, Hadhramout University, Mukalla 50511, Yemen;* orcid.org/0000-0002-7616-7814; Email: a.alshanini@hu.edu.ye

https://doi.org/10.1021/acsomega.3c04543
ACS Omega 2023, 8, 30681−30693

Muhammad Ikram − *Solar Cell Applications Research Lab, Department of Physics, Government College University Lahore, Lahore, Punjab 54000, Pakistan;* orcid.org/0000-0001-7741-789X; Email: dr.muhammadikram@gcu.edu.pk

Authors

Iram Shahzadi − *Punjab University College of Pharmacy, Allama Iqbal Campus, University of the Punjab, Lahore 54000 Punjab, Pakistan*

Muhammad Aqeel − *Department of Physics, The University of Gothenburg, 405 30 Gothenburg, Sweden*

Ali Haider − *Department of Clinical Sciences, Faculty of Veterinary and Animal Sciences, Muhammad Nawaz Shareef University of Agriculture, Multan 66000 Punjab, Pakistan*

Sadia Naz − *Tianjin Institute of Industrial Biotechnology, Chinese Academy of Sciences, Tianjin 300308, China*

Muhammad Imran − *Department of Chemistry, Government College University Faisalabad, Sahiwal, Punjab 57000, Pakistan*

Anum Shahzadi − *Faculty of Pharmacy, The University of Lahore, Lahore, Punjab 54000, Pakistan*

Thamraa Alshahrani − *Department of Physics, College of Sciences, Princess Nourah bint Abdulrahman University (PNU), Riyadh 11671, Saudi Arabia*

Complete contact information is available at: https://pubs.acs.org/10.1021/acsomega.3c04543

Notes

The authors declare no competing financial interest.

■ ACKNOWLEDGMENTS

The authors thank Higher Education Commission Pakistan through NRPU # 20-17615 for financial support. This research was funded by the Princess Nourah bint Abdulrahman University Researchers Supporting Project number (PNURSP2023R1) and Princess Nourah bint Abdulrahman University, Riyadh, Saudi Arabia.

■ REFERENCES

(1) Kim, S. Y.; Hong, K.; Lee, J. L.; Choi, K. H.; Song, K. H.; Ahn, K. C. Enhancement of physical properties of indium tin oxide deposited by super density arc plasma ion plating by O2 plasma treatment. *Solid-State Electron.* **2008**, *52*, 1−6.

(2) Yang, Z.; Huang, Y.; Chen, G.; Guo, Z.; Cheng, S.; Huang, S. Ethanol gas sensor based on Al-doped ZnO nanomaterial with many gas diffusing channels. *Sens. Actuators, B* **2009**, *140*, 549−556.

(3) Aksoy, S.; Caglar, Y.; Ilican, S.; Caglar, M. Effect of heat treatment on physical properties of CdO films deposited by sol−gel method. *Int. J. Hydrogen Energy* **2009**, *34*, 5191−5195.

(4) Waghulade, R. B.; Patil, P. P.; Pasricha, R. Synthesis and LPG sensing properties of nanosized cadmium oxide. *Talanta* **2007**, *72*, 594−599.

(5) Yan, M.; Lane, M.; Kannewurf, C. R.; Chang, R. P. Highly conductive epitaxial CdO thin films prepared by pulsed laser deposition. *Appl. Phys. Lett.* **2001**, *78*, 2342−2344.

(6) Santos-Cruz, J.; Torres-Delgado, G.; Castanedo-Pérez, R.; Jiménez-Sandoval, S.; Márquez-Marín, J.; Zelaya-Angel, O. Au−Cu/p−CdTe/n−CdO/glass-type solar cells. *Sol. Energy Mater. Sol. Cells* **2006**, *90*, 2272−2279.

(7) Soltani, R.; Pelalak, R.; Pishnamazi, M.; Marjani, A.; Albadarin, A. B.; Sarkar, S. M.; Shirazian, S. A novel and facile green synthesis method to prepare LDH/MOF nanocomposite for removal of Cd (II) and Pb (II). *Sci. Rep.* **2021**, *11*, 1609.

(8) Zhao, Z.; Morel, D. L.; Ferekides, C. S. Electrical and optical properties of tin-doped CdO films deposited by atmospheric metalorganic chemical vapor deposition. *Thin Solid Films* **2002**, *413*, 203−211.

(9) Dakhel, A. A. Transparent conducting properties of samarium-doped CdO. *J. Alloys Compd.* **2009**, *475*, 51−54.

(10) Dakhel, A. A. Influence of dysprosium doping on the electrical and optical properties of CdO thin films. *Sol. Energy* **2009**, *83*, 934−939.

(11) Ahmad, T.; Khatoon, S.; Coolahan, K.; Lofland, S. E. Solvothermal synthesis, optical and magnetic properties of nano-crystalline Cd1− xMnxO (0.04< x= 0.10) solid solutions. *J. Alloys Compd.* **2013**, *558*, 117−124.

(12) Dakhel, A. A.; El-Hilo, M.; Bououdina, M. Cu-codoping for the enhancement of ferromagnetism of Fe-doped CdO nanopowders. *J. Supercond. Novel Magn.* **2014**, *27*, 2089−2095.

(13) Yayapao, O.; Thongtem, T.; Phuruangrat, A.; Thongtem, S. Synthesis and characterization of highly efficient Gd doped ZnO photocatalyst irradiated with ultraviolet and visible radiations. *Mater. Sci. Semicond. Process.* **2015**, *39*, 786−792.

(14) Rajesh, N.; Kannan, J. C.; Krishnakumar, T.; Bonavita, A.; Leonardi, S. G.; Neri, G. Microwave irradiated Sn-substituted CdO nanostructures for enhanced CO2 sensing. *Ceram. Int.* **2015**, *41*, 14766−14772.

(15) Tawfik, W. Z.; Esmat, M.; El-Dek, S. I. Drastic improvement in magnetization of CdO nanoparticles by Fe doping. *Appl. Nanosci.* **2017**, *7*, 863−870.

(16) Phatak, G.; Lal, R. Deposition and properties of cadmium oxide films by activated reactive evaporation. *Thin Solid Films* **1994**, *245*, 17−26.

(17) Soltani, R.; Pelalak, R.; Pishnamazi, M.; Marjani, A.; Sarkar, S. M.; Albadarin, A. B.; Shirazian, S. Novel bimodal micro-mesoporous Ni50Co50-LDH/UiO-66-NH2 nanocomposite for Tl (I) adsorption. *Arabian J. Chem.* **2021**, *14*, 103058.

(18) Ferro, R.; Rodrıguez, J. A. Some physical properties of F-doped CdO thin films deposited by spray pyrolysis. *Thin Solid Films* **1999**, *347*, 295−298.

(19) Ranjbar, Z. R.; Morsali, A. Ultrasound assisted syntheses of a nano-structured two-dimensional mixed-ligand cadmium (II) coordination polymer and direct thermolyses for the preparation of cadmium (II) oxide nanoparticles. *Polyhedron* **2011**, *30*, 929−934.

(20) Phuruangrat, A.; Wannapop, S.; Sakhon, T.; Kuntalue, B.; Thongtem, T.; Thongtem, S. Characterization and photocatalytic properties of BiVO4 synthesized by combustion method. *J. Mol. Struct.* **2023**, *1274*, 134420.

(21) Soltani, R.; Marjani, A.; Shirazian, S. Facile one-pot synthesis of thiol-functionalized mesoporous silica submicrospheres for Tl (I) adsorption: Isotherm, kinetic and thermodynamic studies. *J. Hazard. Mater.* **2019**, *371*, 146−155.

(22) Li, X. F.; Cao, Y.; Sui, Y. R.; Yang, J. H.; Yue, Y. G.; Zhang, Q.; Liu, X. Y.; Gao, M.; Lang, J. H.; Li, X. Y. Structure and optical properties of ternary ZnCdO nanopowder synthesized by sol−gel method. *Superlattices Microstruct.* **2014**, *69*, 187−193.

(23) Bokov, D.; Turki Jalil, A.; Chupradit, S.; Suksatan, W.; Javed Ansari, M.; Shewael, I. H.; Valiev, G. H.; Kianfar, E. Nanomaterial by sol-gel method: synthesis and application. *Adv. Mater. Sci. Eng.* **2021**, *2021*, 5102014.

(24) Siriwong, P.; Thongtem, T.; Phuruangrat, A.; Thongtem, S. Hydrothermal synthesis, characterization, and optical properties of wolframite ZnWO 4 nanorods. *CrystEngComm* **2011**, *13*, 1564−1569.

(25) Pinchujit, S.; Phuruangrat, A.; Wannapop, S.; Sakhon, T.; Kuntalue, B.; Thongtem, T.; Thongtem, S. Synthesis and characterization of heterostructure Pt/Bi2WO6 nanocomposites with enhanced photodegradation efficiency induced by visible radiation. *Solid State Sci.* **2022**, *134*, 107064.

(26) Shad, N. A.; Sajid, M. M.; Haq, A. U.; Amin, N.; Imran, Z.; Anwar, H.; Ali, K.; Hussain, Z.; Younus, A.; Javed, Y. Photocatalytic Investigation of Cadmium Oxide Nanosheets Prepared by Hydrothermal Method. *Arabian J. Sci. Eng.* **2019**, *44*, 6669−6675.

(27) Aqeel, M.; Anjum, S.; Imran, M.; Ikram, M.; Majeed, H.; Naz, M.; Ali, S.; Ahmad, M. A. TiO2@ RGO (reduced graphene oxide) doped nanoparticles demonstrated improved photocatalytic activity. *Mater. Res. Express* **2019**, *6*, 086215.
(28) Pascariu, P.; Gherasim, C.; Airinei, A. Metal Oxide Nanostructures (MONs) as Photocatalysts for Ciprofloxacin Degradation. *Int. J. Mol. Sci.* **2023**, *24*, 9564.
(29) Ezealigo, U. S.; Ezealigo, B. N.; Aisida, S. O.; Ezema, F. I. Iron oxide nanoparticles in biological systems: Antibacterial and toxicology perspective. *JCIS Open* **2021**, *4*, 100027.
(30) Shannon, R. D. Revised effective ionic radii and systematic studies of interatomic distances in halides and chalcogenides. *Acta Crystallogr., Sect. A: Cryst. Phys., Diffr., Theor. Gen. Crystallogr.* **1976**, *32*, 751−767.
(31) Tadjarodi, A.; Imani, M.; Kerdari, H. Experimental design to optimize the synthesis of CdO cauliflower-like nanostructure and high performance in photodegradation of toxic azo dyes. *Mater. Res. Bull.* **2013**, *48*, 935−942.
(32) Antosoly, D.; Ilangovan, S.; Suganya, M.; Balamurugan, S.; Balu, A. R. Optical and magnetic properties of CdO thin films doped with Ba2+ (cation) ions. *Mater. Res. Innovations* **2018**, *22*, 237−241.
(33) Pandey, N.; Cascella, M. Beta lactam antibiotics. In *StatPearls [Internet]*; StatPearls Publishing, 2022.
(34) Paterson, D. L.; Ko, W. C.; Von Gottberg, A.; Casellas, J. M.; Mulazimoglu, L.; Klugman, K. P.; Bonomo, R. A.; Rice, L. B.; McCormack, J. G.; Yu, V. L. Outcome of cephalosporin treatment for serious infections due to apparently susceptible organisms producing extended-spectrum β-lactamases: implications for the clinical microbiology laboratory. *J. Clin. Microbiol.* **2001**, *39*, 2206−2212.
(35) Ellsworth, B. A.; Tom, N. J.; Bartlett, P. A. Synthesis and evaluation of inhibitors of bacterial D-alanine: D-alanine ligases. *Chem. Biol.* **1996**, *3*, 37−44.
(36) Heath, R. J.; Rock, C. O. Enoyl-acyl carrier protein reductase (fabI) plays a determinant role in completing cycles of fatty acid elongation in Escherichia coli. *J. Biol. Chem.* **1995**, *270*, 26538−26542.
(37) Lim, D.; Strynadka, N. C. Structural basis for the β lactam resistance of PBP2a from methicillin-resistant Staphylococcus aureus. *Nat. Struct. Biol.* **2002**, *9*, 870−876.
(38) Alexander, J. A. N.; Chatterjee, S. S.; Hamilton, S. M.; Eltis, L. D.; Chambers, H. F.; Strynadka, N. C. Structural and kinetic analyses of penicillin-binding protein 4 (PBP4)-mediated antibiotic resistance in Staphylococcus aureus. *J. Biol. Chem.* **2018**, *293*, 19854−19865.
(39) Schiebel, J.; Chang, A.; Shah, S.; Lu, Y.; Liu, L.; Pan, P.; Hirschbeck, M. W.; Tareilus, M.; Eltschkner, S.; Yu, W.; et al. Rational design of broad spectrum antibacterial activity based on a clinically relevant enoyl-acyl carrier protein (ACP) reductase inhibitor. *J. Biol. Chem.* **2014**, *289*, 15987−16005.
(40) Abagyan, R.; Totrov, M. Biased probability Monte Carlo conformational searches and electrostatic calculations for peptides and proteins. *J. Mol. Biol.* **1994**, *235*, 983−1002.
(41) Systèmes, D. *Biovia, discovery studio modeling environment*; Dassault Systèmes Biovia: San Diego, CA, USA, 2016.
(42) Nallendran, R.; Selvan, G.; Balu, A. R. CdO-Fe3O4 nanocomposite with enhanced magnetic and photocatalytic properties. *Mater. Sci.* **2019**, *37*, 100−107.
(43) Ali Ahmad, S. O.; Ikram, M.; Imran, M.; Naz, S.; Ul-Hamid, A.; Haider, A.; Shahzadi, A.; Haider, J. Novel prism shaped C 3 N 4-doped Fe@ Co 3 O 4 nanocomposites and their dye degradation and bactericidal potential with molecular docking study. *RSC Adv.* **2021**, *11*, 23330−23344.
(44) Sankarasubramanian, K.; Soundarrajan, P.; Sethuraman, K.; Ramamurthi, K. Chemical spray pyrolysis deposition of transparent and conducting Fe doped CdO thin films for ethanol sensor. *Mater. Sci. Semicond. Process.* **2015**, *40*, 879−884.
(45) Ranjithkumar, R.; Albert Irudayaraj, A.; Jayakumar, G.; Dhayal Raj, A.; Karthick, S.; Vinayagamoorthy, R. Synthesis and properties of CdO and Fe doped CdO nanoparticles. *Mater. Today: Proc.* **2016**, *3*, 1378−1382.
(46) Balamurugan, S.; Balu, A. R.; Usharani, K.; Suganya, M.; Anitha, S.; Prabha, D.; Ilangovan, S. Synthesis of CdO nanopowders by a simple soft chemical method and evaluation of their antimicrobial activities. *Pac. Sci. Rev.* **2016**, *18*, 228−232.
(47) Sivakumar, S.; Venkatesan, A.; Soundhirarajan, P.; Khatiwada, C. P. Thermal, structural, functional, optical and magnetic studies of pure and Ba doped CdO nanoparticles. *Spectrochim. Acta, Part A* **2015**, *151*, 760−772.
(48) Ravikumar, M.; Chandramohan, R.; Kumar, K. D. A.; Valanarasu, S.; Ganesh, V.; Shkir, M.; Alfaify, S.; Kathalingam, A. Effect of Nd doping on structural and opto-electronic properties of CdO thin films fabricated by a perfume atomizer spray method. *Bull. Mater. Sci.* **2019**, *42*, 8.
(49) Khan, T. M.; Shahid, T.; Zakria, M.; Shakoor, R. I. Optoelectronic properties and temperature dependent mechanisms of composite-hydroxide-mediated approach for the synthesis of CdO nanomaterials. *Electron. Mater. Lett.* **2015**, *11*, 366−373.
(50) Schaack, G.; Uhle, N. Raman spectra in doped cadmium oxide. *Solid State Commun.* **1976**, *19*, 315−318.
(51) Thema, F. T.; Beukes, P.; Gurib-Fakim, A.; Maaza, M. Green synthesis of Monteponite CdO nanoparticles by Agathosma betulina natural extract. *J. Alloys Compd.* **2015**, *646*, 1043−1048.
(52) Benhaliliba, M.; Benouis, C. E.; Tiburcio-Silver, A.; Yakuphanoglu, F.; Avila-Garcia, A.; Tavira, A.; Trujillo, R. R.; Mouffak, Z. Luminescence and physical properties of copper doped CdO derived nanostructures. *J. Lumin.* **2012**, *132*, 2653−2658.
(53) Dong, W.; Zhu, C. Optical properties of surface-modified CdO nanoparticles. *Opt. Mater.* **2003**, *22*, 227−233.
(54) Kumar, S.; Ojha, A. K.; Walkenfort, B. Cadmium oxide nanoparticles grown in situ on reduced graphene oxide for enhanced photocatalytic degradation of methylene blue dye under ultraviolet irradiation. *J. Photochem. Photobiol., B* **2016**, *159*, 111−119.
(55) Moeen, S.; Ikram, M.; Haider, A.; Haider, J.; Ul-Hamid, A.; Nabgan, W.; Shujah, T.; Naz, M.; Shahzadi, I. Comparative Study of Sonophotocatalytic, Photocatalytic, and Catalytic Activities of Magnesium and Chitosan-Doped Tin Oxide Quantum Dots. *ACS Omega* **2022**, *7*, 46428−46439.
(56) Endres, S. C.; Ciacchi, L. C.; Mädler, L. A review of contact force models between nanoparticles in agglomerates, aggregates, and films. *J. Aerosol Sci.* **2021**, *153*, 105719.
(57) Khan, A. U. H.; Liu, Y.; Naidu, R.; Fang, C.; Dharmarajan, R.; Shon, H. Interactions between zinc oxide nanoparticles and hexabromocyclododecane in simulated waters. *Environ. Technol. Innovation* **2021**, *24*, 102078.
(58) Sui, Y.; Yue, Y.; Song, Y.; Cao, Y.; Yao, B.; Lang, J.; Li, X.; Yang, J. Effects of Cd concentration on microstructure and optical properties of the ternary Zn1− xCdxO alloy thin films synthesized by magnetron sputtering. *Mater. Res. Bull.* **2015**, *70*, 348−353.
(59) Saravanakumar, K.; Muthuraj, V.; Jeyaraj, M. The design of novel visible light driven Ag/CdO as smart nanocomposite for photodegradation of different dye contaminants. *Spectrochim. Acta, Part A* **2018**, *188*, 291−300.
(60) Kumar, S.; Ahmed, B.; Ojha, A. K.; Das, J.; Kumar, A. Facile synthesis of CdO nanorods and exploiting its properties towards supercapacitor electrode materials and low power UV irradiation driven photocatalysis against methylene blue dye. *Mater. Res. Bull.* **2017**, *90*, 224−231.
(61) Kumar, S.; Layek, S.; Yashpal, M.; Ojha, A. K. Room temperature ferromagnetism in undoped and Mn doped CdO nanostructures. *J. Magn. Magn. Mater.* **2015**, *393*, 555−561.
(62) Senthil, S.; Srinivasan, S.; Thangeeswari, T.; Ratchagar, V. Enrichment of optical, magnetic and photocatalytic properties in PVP capped CdO/SnO 2 nanocomposites synthesized by microwave irradiation method. *J. Mater. Sci.: Mater. Electron.* **2019**, *30*, 19841−19853.
(63) Manickathai, K.; Viswanathan, S. K.; Alagar, M. Synthesis and characterization of CdO and CdS nanoparticles. *Indian J. Pure Appl. Phys.* **2008**, *46*, 561.

https://doi.org/10.1021/acsomega.3c04543
ACS Omega 2023, 8, 30681−30693

(64) Mandal, R. K.; Saha, P.; Majumder, T. P. Structural, optical characterization of the synthesized Fe doped CdO Nano particles, its application as a promising photocatalyst for degradation of the hazardous Methyl violet dye. *Optik* **2021**, *246*, 167795.
(65) Tadjarodi, A.; Imani, M.; Kerdari, H.; Bijanzad, K.; Khaledi, D.; Rad, M. Preparation of CdO rhombus-like nanostructure and its photocatalytic degradation of azo dyes from aqueous solution. *Nanomater. Nanotechnol.* **2014**, *4*, 16.
(66) Bharti, D. B.; Bharati, A. V. Photocatalytic degradation of Alizarin Red dye under visible light using ZnO & CdO nanomaterial. *Optik* **2018**, *160*, 371−379.
(67) Shad, N. A.; Sajid, M. M.; Haq, A. U.; Amin, N.; Imran, Z.; Anwar, H.; Ali, K.; Hussain, Z.; Younus, A.; Javed, Y. Photocatalytic investigation of cadmium oxide nanosheets prepared by hydrothermal method. *Arabian J. Sci. Eng.* **2019**, *44*, 6669−6675.
(68) Ikram, M.; Jamal, F.; Haider, A.; Dilpazir, S.; Shujah, T.; Naz, M.; Imran, M.; Ul-Hamid, A.; Shahzadi, I.; Ullah, H.; Nabgan, W.; et al. Efficient Photocatalytic Dye Degradation and Bacterial Inactivation by Graphitic Carbon Nitride and Starch-Doped Magnesium Hydroxide Nanostructures. *ACS Omega* **2022**, *7*, 39998−40008.
(69) Bilal, M.; Ikram, M.; Shujah, T.; Haider, A.; Naz, S.; Ul-Hamid, A.; Naz, M.; Haider, J.; Shahzadi, I.; Nabgan, W. Chitosan-Grafted Polyacrylic Acid-Doped Copper Oxide Nanoflakes Used as a Potential Dye Degrader and Antibacterial Agent: In Silico Molecular Docking Analysis. *ACS Omega* **2022**, *7*, 41614−41626.
(70) Li, Z.; Zhang, Z.; Wang, L.; Meng, X. Bismuth chromate (Bi2CrO6): A promising semiconductor in photocatalysis. *J. Catal.* **2020**, *382*, 40−48.
(71) Shahzadi, A.; Moeen, S.; Khan, A. D.; Haider, A.; Haider, J.; Ul-Hamid, A.; Nabgan, W.; Shahzadi, I.; Ikram, M.; Al-Shanini, A. La-Doped CeO2 Quantum Dots: Novel Dye Degrader, Antibacterial Activity, and In Silico Molecular Docking Analysis. *ACS Omega* **2023**, *8*, 8605−8616.
(72) Kim, S. P.; Choi, M. Y.; Choi, H. C. Photocatalytic activity of SnO2 nanoparticles in methylene blue degradation. *Mater. Res. Bull.* **2016**, *74*, 85−89.
(73) Demirci, S.; Dikici, T.; Yurddaskal, M.; Gultekin, S.; Toparli, M.; Celik, E. Synthesis and characterization of Ag doped TiO2 heterojunction films and their photocatalytic performances. *Appl. Surf. Sci.* **2016**, *390*, 591−601.
(74) Ren, P.; Song, M.; Lee, J.; Zheng, J.; Lu, Z.; Engelhard, M.; Yang, X.; Li, X.; Kisailus, D.; Li, D. Edge dislocations induce improved photocatalytic efficiency of colored TiO2. *Adv. Mater. Interfaces* **2019**, *6*, 1901121.
(75) Qamar, M.; Yamani, Z. H.; Gondal, M. A.; Alhooshani, K. Synthesis and comparative photocatalytic activity of Pt/WO3 and Au/WO3 nanocomposites under sunlight-type excitation. *Solid State Sci.* **2011**, *13*, 1748−1754.
(76) Uribe-López, M. C.; Hidalgo-López, M. C.; López-González, R.; Frías-Márquez, D. M.; Núñez-Nogueira, G.; Hernández-Castillo, D.; Alvarez-Lemus, M. A. Photocatalytic activity of ZnO nanoparticles and the role of the synthesis method on their physical and chemical properties. *J. Photochem. Photobiol., A* **2021**, *404*, 112866.
(77) Sanad, M. M.; Farahat, M. M.; El-Hout, S. I.; El-Sheikh, S. M. Preparation and characterization of magnetic photocatalyst from the banded iron formation for effective photodegradation of methylene blue under UV and visible illumination. *J. Environ. Chem. Eng.* **2021**, *9*, 105127.
(78) Nallendran, R.; Selvan, G.; Balu, A. R. Photoconductive and photocatalytic properties of CdO−NiO nanocomposite synthesized by a cost effective chemical method. *J. Mater. Sci.: Mater. Electron.* **2018**, *29*, 11384−11393.
(79) Haider, A.; Ijaz, M.; Imran, M.; Naz, M.; Majeed, H.; Khan, J. A.; Ali, M. M.; Ikram, M. Enhanced bactericidal action and dye degradation of spicy roots' extract-incorporated fine-tuned metal oxide nanoparticles. *Appl. Nanosci.* **2020**, *10*, 1095−1104.
(80) Qumar, U. S. M. A. N.; Ikram, M.; Imran, M.; Haider, A.; Ul-Hamid, A.; Haider, J.; Riaz, K. N.; Ali, S. Synergistic effect of Bi-doped exfoliated MoS 2 nanosheets on their bactericidal and dye degradation potential. *Dalton Trans.* **2020**, *49*, 5362−5377.
(81) Fang, W.; Chaofa Xu, C. X.; Zheng, J.; Chen, G.; Jiang, K. Fabrication of Cu−Ag bimetal nanotube-based copper silicates for enhancement of antibacterial activities. *RSC Adv.* **2015**, *5*, 39612−39619.
(82) Shahzadi, I.; Islam, M.; Saeed, H.; Haider, A.; Shahzadi, A.; Haider, J.; Ahmed, N.; Ul-Hamid, A.; Nabgan, W.; Ikram, M.; Rathore, H. A. Formation of biocompatible MgO/cellulose grafted hydrogel for efficient bactericidal and controlled release of doxorubicin. *Int. J. Biol. Macromol.* **2022**, *220*, 1277−1286.
(83) Shahzadi, I.; Islam, M.; Saeed, H.; Shahzadi, A.; Haider, J.; Haider, A.; Imran, M.; Rathore, H. A.; Ul-Hamid, A.; Nabgan, W.; Ikram, M. Facile synthesis of copolymerized cellulose grafted hydrogel doped calcium oxide nanocomposites with improved antioxidant activity for anti-arthritic and controlled release of doxorubicin for anti-cancer evaluation. *Int. J. Biol. Macromol.* **2023**, *235*, 123874.
(84) Ikram, M.; Abbasi, S.; Haider, A.; Naz, S.; Ul-Hamid, A.; Imran, M.; Haider, J.; Ghaffar, A. Bimetallic Ag/Cu incorporated into chemically exfoliated MoS2 nanosheets to enhance its antibacterial potential: in silico molecular docking studies. *Nanotechnology* **2020**, *31*, 275704.
(85) Nasrullah, M.; Gul, F. Z.; Hanif, S.; Mannan, A.; Naz, S.; Ali, J. S.; Zia, M. Green and chemical syntheses of CdO NPs: a comparative study for yield attributes, biological characteristics, and toxicity concerns. *ACS Omega* **2020**, *5*, 5739−5747.

https://doi.org/10.1021/acsomega.3c04543
ACS Omega 2023, 8, 30681−30693